

Fault Ratio Enriched Anomaly Detection and Discrimination in a PV System using a Fault Detector-Array Combiner Box

J. Prasanth Ram, *Member, IEEE*, Young-Jin Kim, *Senior Member, IEEE*, and João P. S. Catalão, *Fellow, IEEE*

Abstract—Photovoltaic (PV) power generation is susceptible to various permanent electrical faults, including line-to-line (LL), line-to-ground (LG), and open-circuit (OC) faults. Additionally, non-catastrophic, temporary shading faults can also occur. These faults can lead to changes in the I-V characteristics and cause a shift in the maximum power point (MPP). Permanent faults such as LL/LG and OC can significantly alter the array's open circuit voltage and short circuit current. This research proposes a novel sensor-less approach for detecting, discriminating, and locating different faults in a PV array. The proposed approach utilizes the mandatory Maximum Power Point Tracking (MPPT) reference to assess the likelihood of fault occurrence. It then analyzes the altered I-V characteristics to discriminate and locate the fault location within the PV array. To facilitate fault detection and categorization, a new Fault Detector-Array Combiner Box (FD-ACB) with power electronic switches has been developed. The effectiveness of the proposed algorithm is evaluated using a test setup consisting of three 4x4 sub-arrays. Detailed case studies involving LL/LG, OC, and shade faults are presented. The results demonstrate that the sensor-less FD-ACB setup has the potential to find (i) undetected and undiagnosed LL/LG and OC faults, (ii) discriminate shade and permanent faults, and (iii) locate the faulty PV sub-array vulnerable to permanent faults.

Index Terms—PV faults, maximum power point (MPP), LL (line-to-line), LG (line-to-ground), and FD-ACB (fault detector-array combiner box).

NOMENCLATURE

A. Acronyms

CFR	current fault ratio
FD-ACB	fault detector-array combiner box
GFPD	ground fault protection device
LG	line-to-ground
LL	line-to-line
MPP	maximum power point
OC	open circuit
OCPD	over current protection device
P&O	perturb and observe
PS	partial shade
PV	photovoltaic
RPP	right power peak
VFR	voltage fault ratio

B. Parameters and variables

D_{MPP}	duty value at MPP
D_{ref}	reference duty ratio (0.1) of P&O tracking
$D_{ref-MPP}$	load line reference at MPP duty value
I_f -ratio	current fault ratio
$I_{MPP-global}$	predicted MPP current from global sub-array current
I_{OC}	current at open circuit condition
$I_{OC-fault}$	current value at OC fault
I_{SC}	short circuit current
$I_{sPV,i-array}$	current value of i^{th} sub-array
$I_{sPV,i-MPP}$	current value of i^{th} sub-array at MPP
$I_{sPV,i-MPP,ref}$	reference voltage of i^{th} sub-array at MPP
k	total number of sub-arrays in the PV arrangement
R_L	load resistance value
$R_{MPP,i}$	resistance of i^{th} sub-array at MPP
S_{Li}	load switch of i^{th} sub-array in FD-ACB
S_{PVi}	array switch of i^{th} sub-array
V_f -ratio	voltage fault ratio
$V_{LL} \& V_{LG}$	voltage of LL and LG faults
$V_{LL-array}$	LL voltage of the sub-array
$V_{MPP-global}$	predicted MPP voltage from global sub-array voltage
V_{OC}	open circuit voltage
$V_{sPV,i-array}$	voltage value of i^{th} sub-array
$V_{sPV,i-MPP}$	MPP voltage of i^{th} sub-array
$V_{sPV,i-MPP,ref}$	reference voltage of i^{th} sub-array at MPP
$V_{sPV-global}$	global voltage of all sub-array
$V_{sPV-RPP}$	voltage of sub-array at the right power peak
V_{UNF}, I_{UNF}	voltage and current at normal condition
ΔV	voltage range to determine the fault

I. INTRODUCTION

ENERGY crisis in the modern power sector is a huge apprehension, where integration of renewables into the power grid has taken a secured leap to build a resilient, sustainable, and eco-friendly power system [1]. In particular, photovoltaic (PV) power generation has taken a lead among renewables to assure the fast-growing energy demand. However, the occurrence of permanent and temporary faults in PV systems is prominent and it demands immediate care to be attenuated for sustained operation.

Conventional PV arrays typically incorporate over-current protection devices (OCPD) and ground-fault protection devices (GFPD) to safeguard against line-to-line (LL) and line-to-ground (LG) faults [2]. However, existing protection schemes often fail to detect PV faults due to several reasons. These include the presence of power conditioning units and blocking diodes, misconceptions regarding fault occurrence

The work of J. Prasanth Ram is support by was supported by the National Research Foundation of Korea funded by the Ministry of Science and ICT under Grant 2020H1D3A1A04079991. (*Corresponding Author: Y. J. Kim*)

J. P. Ram and Y. Kim are with the Department of Electrical Engineering, Pohang University of Science and Technology, Pohang 37673, South Korea (e-mails: drjppram@postech.ac.kr, powersys@postech.ac.kr).

J.P.S. Catalão is with the Research Center for Systems and Technologies (SYSTEC), Advanced Production and Intelligent Systems Associate Laboratory (ARISE), Faculty of Engineering, University of Porto, 4200-465 Porto, Portugal (e-mail: catalao@fe.up.pt).

under low irradiation conditions (e.g., blind spots), and false operation of MPP trackers (MPPT). Additionally, partial shading (PS) is a temporary fault that can occur in a PV array, resulting in multiple power peaks in P - V characteristics and steps in I - V characteristics. Unlike permanent faults, PS events are non-catastrophic but require momentary adjustments in the MPPT algorithm to operate at the global maximum power point (GMPP). Thus, apart from fault detection, discrimination becomes essential to achieve optimal efficiency.

Numerous algorithms have been proposed in the literature to detect abnormalities in PV arrays, and a review of these methods is presented here. For fault identification in PV systems, thermography-based MPPT schemes [3], earth capacitance measurement (ECM) methods [4], and time-domain reflectometry (TDR) methods [5] have been proposed as predecessors for diagnosing faults in PV arrays. However, these methods have limitations such as device aging, the need for thermal cameras, offline operation of ECM methods, and mismatched connections of PV strings, which hinder the development of cost-effective and fault-tolerant PV systems. In contrast, sensor-based PV models have gained considerable interest among researchers for fault diagnosis in PV arrays. Research studies have explored the placement of modular-level voltage sensors [6], wireless sensors [7], and current sensors [8] for fault detection in PV systems. Furthermore, the restructured use of voltage and current sensors at the individual string level has also been presented for detecting catastrophic faults [9], [10]. Although sensor-based methods offer accurate fault diagnosis, their drawback lies in the high initial cost associated with the sensors.

In [11], a detailed DC analysis was conducted to analyze the behaviors of temporary faults and (LL)/ (LG) faults. Another work [12] focused on irradiation-independent detection of LG faults using advanced time-domain reflectometry (TDR). However, this approach was limited to LG faults and did not address the discrimination of temporary faults. In contrast, a mismatch fault diagnosis technique was proposed in [13] to identify shadows, hotspots, and cell cracks. While this method is effective for verifying the health of PV systems, it does not address the diagnosis of undetected faults. In [14], a voltage-current trajectory-based fault monitoring technique was experimented with, but it lacked clarity in identifying LL/LG or shade faults.

Recently, fault diagnosis algorithms implemented using MPPT controllers have gained significant attention due to their cost-effectiveness, sensor-less nature, and lower complexity. These algorithms leverage the information extracted from sensor values to operate PV arrays at the MPP regions and discriminate faulty conditions. For instance, an online fault detection scheme using wavelet packets was proposed in [15], but it required a large number of data points to diagnose fault occurrences. Another sensorless fault detection algorithm based on the occurrence of the right power peak (RPP) in shading cases was proposed in [16], but its voltage reference formulation for discriminating LL/LG faults and shading faults had limited implications for real-time implementation.

Distinct from the earlier schemes, a fault detection algorithm based on the operating condition of the PV inverter was implemented in [17]. However, the rapid switching in the

inverter raised the probability of semiconductor switching failure in the converter systems. Additionally, a complete dataset of faulty I - V characteristics was required as a prerequisite, resulting in the need for a large volume of data. In [18], an interleaved boost converter-based fault detection scheme to eliminate open circuit (OC) faults is experimented for a PV array. However, this approach did not address vulnerable LL/LG faults. In another work [19], switching devices were deployed to develop a fault-tolerant PV system for various environmental conditions, but it suffered from the same drawback as the previous work [18].

The use of data-driven fuzzy tools and artificial intelligence (AI) algorithms has also gained prominence in PV fault diagnosis research. Neuro-fuzzy frameworks [20], unique fuzzy logic tools [21], multi-layer perceptron neural networks [22], and unsupervised learning techniques [23] have been employed for successful PV fault diagnosis. However, these approaches often require extensive data training and demand high-end processors. Moreover, the application of AI in real-time on-site operation has yet to be extensively explored. Due to recent advancements in PV technologies, fault ratio-based techniques have emerged, incorporating MPP ratios, environmental factors, remote supervision, and S-transform analysis [24]–[28]. However, all these techniques have limited scope for implementation, because the ratios are not totally dependent on specific models. In summary, the existing literature reveals several conclusions in the field of PV fault diagnosis research:

- Online sensor-less PV fault diagnosis schemes are more suitable and cost-effective;
- MPPT-based fault diagnosis schemes are sensor-less and capable of discriminating permanent and temporary faults;
- Techniques based on thresholds and fault ratios that rely on operating voltage and current are crucial for detecting fault occurrences;
- AI-based techniques have a high demand for training data, which is not necessary for instant fault detection schemes.

Given the previous studies, there still exists a significant research gap in discriminating shade, OC, and LL/LG faults, particularly the commercial PV grid-connected inverter systems powered from the DC side with multiple arrays or strings connected to a common DC link. The literature lacks a proposed PV array framework for multiple PV sub-arrays on a larger scale and the discrimination of temporary and permanent faults for multiple arrays connected to a DC side.

To address this gap, this study proposes a new sensorless fault detection method for multiple PV sub-arrays connected to a common DC bus. The reference MPP data of all sub-arrays are used to detect abnormal operations, considering the mandatory obligation of MPP control in PV systems. Exclusive MPP fault ratios are determined through fault studies to identify fault occurrences, which are then confirmed by changes in the open-circuit voltage and short-circuit current. A novel FD-ACB made of power electronic switches is proposed to verify the characteristic changes exhibited by the faulty sub-array, enabling practical applicability. By sequentially switching the FD-ACB, the PV system can recognize LL/LG, OC, and PS faults. The proposed method detects faults by utilizing exclusive fault ratios and verifying their actual I - V characteristics, making it the first of its kind

for PV fault detection. Moreover, the proposed system is capable of detecting, discriminating, and locating faults on a larger scale through a simple two-step process, providing valuable insights into fault occurrences. To be precise, the MCB is tripped in the first step, once the fault ratios are verified, and subsequently, the FD-ACB switching is performed to discriminate fault type. Additionally, the setup also has the potential to isolate the faulty sub-array in the PV system without requiring additional sensor circuitry, resulting in significant economic benefits for large PV arrays. A summary of outcomes and deliverables of the proposed research is provided in the following as highlights.

- New fault ratios have been developed to accurately detect various electrical faults in grid-connected PV systems. These ratios are highly reliable for identifying the occurrence of various faults within the system.
- A novel FD-ACB setup has been proposed and tested to discriminate LL/LG, shade, and OC faults. This setup requires only three samples to determine the nature and behavior of the faults.
- The developed fault ratios and FD-ACB can be readily implemented in commercial PV inverters, offering an advantage in enhancing the overall protection standard.
- Implementation of the proposed research not only improves safety but also reduces capital investment (CAPEX cost) due to its sensorless nature and reduced computational requirements.

The subsequent sections will provide detailed discussions on the fundamentals of PV faults, fault ratio determination, validations with PV faults in a sub-array, and case studies using the test setup.

II. FUNDAMENTALS

A. System Composition and Operation

In Fig.1, a common grid-connected PV system is depicted, featuring three 4×4 PV sub-arrays as an illustrative example. The system comprises multiple strings and sub-arrays connected to DC-DC converters or string converters, which facilitate power delivery to a shared DC bus denoted by the positive and negative rails. At the system's backend, an inverter is employed to interface with the distribution grid.

Each PV string is linked to the converters through the utilization of OCPDs and GFPD fuses. Notably, fault occurrences within each sub-array are visually discerned via a

novel circuitual assembly referred to as the FD-ACB. By employing a fixed resistance (R) and an LED arrangement, this innovative approach eliminates the necessity for conventional fault detection methodologies that rely heavily on sensor-based implementations [9]–[11].

The FD-ACB, constituting load switches ($S_{L1}, S_{L2}, \dots, S_{Ln}$), and array switches ($S_{PV1}, S_{PV2}, \dots, S_{PVn}$) interconnected with the designated load, is an external circuitry component. Consequently, the FD-ACB encompasses ‘ n ’ DC-DC converters and ‘ $n \times 2$ ’ switches to accommodate n sub-arrays.

Each individual sub-array is linked to an MPPT controller equipped with voltage and current sensors, enabling the sub-array to operate at its maximum power point (MPP) under normal, fault, and PS conditions [6]. The MPPT controllers play a pivotal role in triggering the switches of the FD-ACB when fault conditions are detected. Further elucidation regarding the operation and control of the FD-ACB, as well as the significance of the MPPT controllers, will be provided in Section IV of this manuscript. An in-depth explanation concerning the functionality of the FD-ACB, including its operation and control, along with the role of the MPPT controllers, will be elaborated upon in Section IV of the manuscript.

B. MPP Tracking under Normal, Fault, and Shade Conditions

The proposed method for fault detection and discrimination relies on the real-time measurement of voltage and current values obtained through the MPP controllers. This approach allows for the implementation of the proposed method using readily available MPP data commonly found in practical PV systems. Note that MPP operation in commercial PV inverters has a wide operating range, and the proposed fault detection algorithm can be commercialized in this case as well. The MPP tracking of the test PV system is evaluated under various abnormal scenarios, including LL, LG, and OC faults, as well as PS events, as summarized in Table I. Each of these scenarios induces characteristic changes in the I - V characteristics, as previously discussed in [1], [16].

In the MPP tracking process, all PV sub-arrays are assumed to operate using a common P&O algorithm [29]. Typically, the P&O algorithm is employed to track the MPP at a duty cycle of 0.1, corresponding to the CVR. It is worth noting that the proposed fault detection and discrimination method can also be applied to PV systems utilizing the P&O algorithm at a duty cycle of 0.9 (in the CCR) or employing different MPPT

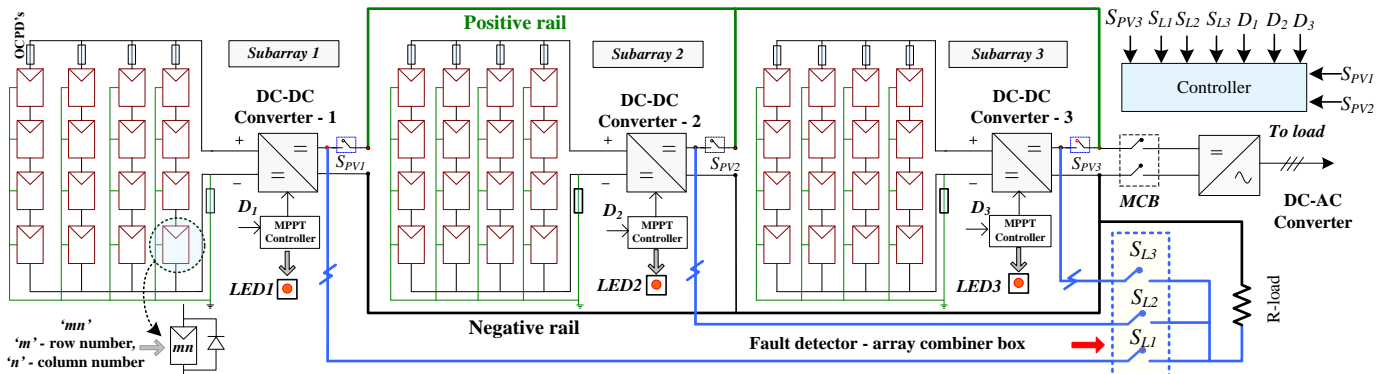


Fig. 1. Common grid-connected PV system, for example, including three sub-arrays, and FD-ACB setup. Each sub-array is equipped with a DC-DC converter, a MPPT controller, and a LED.

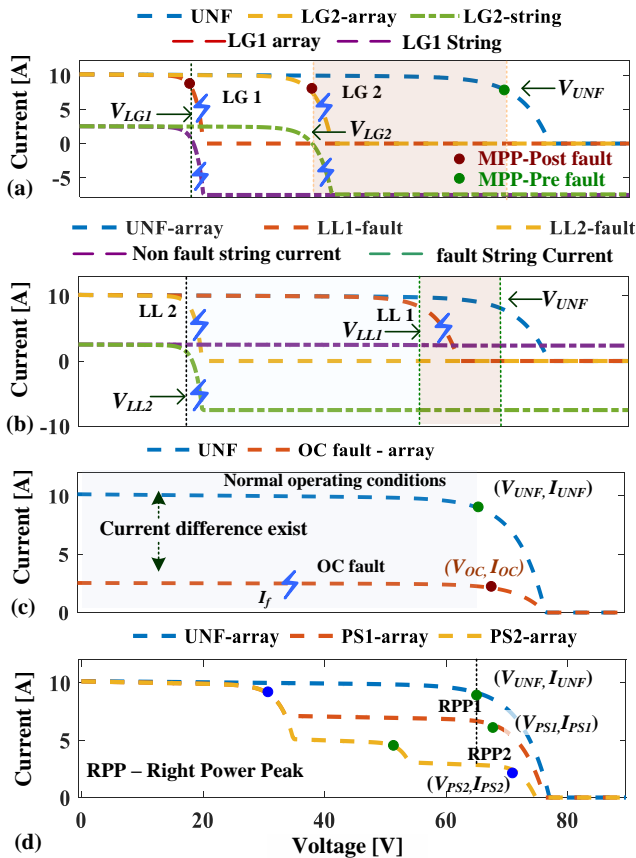


Fig. 2. I - V characteristics of the test PV system: (a) L-G fault (b) L-L fault (c) OC fault and (d) PS event.

algorithms.

Fig.2 illustrates the I - V characteristics of the test PV system under different fault scenarios, namely (a) LG fault, (b) LL fault, (c) OC fault, and (d) PS event. The system is modeled using the S36 shell panel data. It is important to highlight that both inter-string and intra-string LL faults are specifically presented in Fig. 2(b). Additionally, the I - V characteristics under normal operating conditions are included for reference, facilitating a better understanding of the changes that occur during fault conditions. Several key observations can be made from the plots:

- LL, LG, and OC faults are considered permanent faults that lead to a significant reduction in output power, accompanied by a shift in the MPP.
- LL and LG faults exhibit similar characteristics, making them challenging to discriminate from each other.
- LL and LG faults are characterized by a voltage drop compared to the normal operating condition, indicated by $V_{LL} < V_{UNF}$ and $V_{LG} < V_{UNF}$, respectively.
- OC faults result in a reduction of short circuit current I_{SC} compared to the normal operating condition, denoted by $I_{OC} < I_{UNF}$.
- PS events are temporary faults that do not cause a reduction in V_{OC} and I_{SC} .

Further details regarding the behaviors observed during MPP tracking and important insights derived from these characteristics will be discussed in subsequent subsections.

i. LL and LG Faults

Following the PV system configuration depicted in Fig.1, sub-arrays $k = 1$ and 3 are subjected to LL faults, while Sub-array $k = 2$ operates under normal conditions, as indicated in Table I. For understanding, the I - V characteristics of ideal conditions and LL/LG conditions are presented in Fig.3(a). The P&O MPP tracking is initially initiated at 75.5 V and 2.8 A for the normal condition. For the LL fault scenario, the probable MPP is identified as 64.5 V and 9.2 A [1], [16]. The plot in Fig.3(a) also includes the duty ratio tracked from the reference duty cycle ($D_{ref} = 0.1$) to the MPP duty cycle (D_{MPP}), along with the load-line reference denoted as $D_{ref-MPP}$.

Contrastingly, the two sub-arrays experiencing LL faults exhibit MPP values of 51.5 V with 9.4 A and 34.3 V with 9.4 A, respectively. This confirms that the MPP tracking of the faulty sub-arrays leads to a significant reduction in the tracked voltage compared to the normal operating condition. The magnitude of the voltage reduction depends on the location of the LL faults. The same observations can be made for LG faults as well.

ii. OC Faults

In the PV system presented in Fig.1., the OC faults are introduced to Sub-array $k = 3$ at the string level, as specified in Table I. Specifically, two out of four strings in the sub-array are open-circuited, while the other sub-arrays (i.e., $k = 1$ and 2) remain unaffected. Fig.3(b) visually represents the instantaneous effect on the I - V characteristic due to the OC faults. With the P&O algorithm operating at a duty cycle of

TABLE I
FAULT SCENARIOS IN THE TEST PV SYSTEM

No	Abnormal events	Sub-array 1	Sub-array 2	Sub-array 3
1	LL and LG faults	×	×	✓
2	OC faults	×	×	✓
3	PS events	✓	✓	×

✓: fault condition, ×: normal operating condition

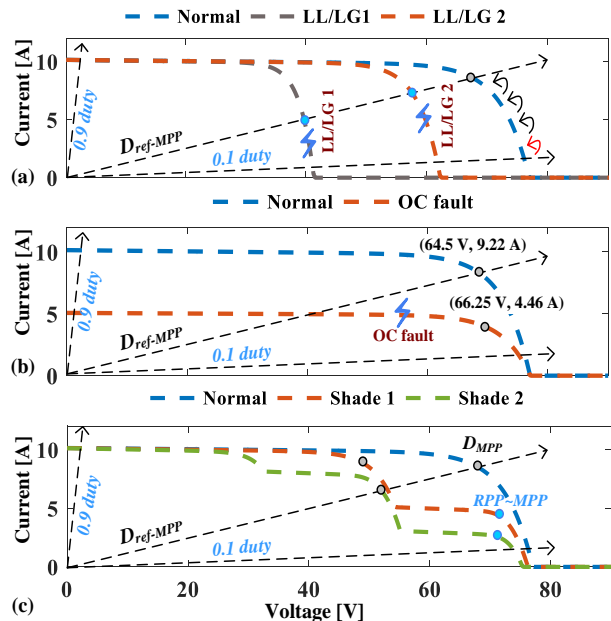


Fig. 3. I - V characteristics of the test PV system for the cases of (a) the L/LG faults, (b) the OC fault, and (c) the partial shading event.

0.1, the MPP value under normal operating conditions is determined as 64.5 V and 9.22 A. In contrast, the sub-array affected by the OC faults exhibits an MPP value of 66.25 V and 4.46 A. This implies that the current in the faulty sub-array is reduced by more than 50% compared to the normal condition. Therefore, the presence of OC faults in a PV system can be detected by measuring the difference in MPP currents between the normal and fault conditions.

iii. PS Events

In Table I, the PS events are considered in two sub-arrays, specifically sub-arrays $k = 1$ and 2, resulting in multiple peaks in the I - V characteristics. Fig. 3(c) illustrates the effect of implementing the P&O algorithm with a duty cycle of 0.1, which settles the MPP controller to the first RPP.

By analyzing the I - V characteristics, the probable settling values of the RPP for the shaded sub-arrays are determined as 69.7 V with 4.68 A and 75.0 V with 1.76 A, respectively. In contrast, under normal operating conditions, the P&O MPP settles at 64.5 V and 9.2 A. Comparing the RPP data, it can be observed that the MPP voltage of the shaded sub-arrays is always higher than that of the normal sub-array. It is important to note that temporary shading events do not cause significant

changes in the open-circuit voltage (V_{OC}) and short-circuit current (I_{SC}), unlike the case of permanent faults such as LL, LG, and OC faults.

iv. Inferences from the MPP Tracking

Based on the detailed observations mentioned above, the following inferences can be made:

- In the case of LL and LG faults, there is a significant deviation in the tracked voltage compared to the voltage during normal operation. The magnitude of the deviation varies depending on the location of the fault.
- For OC faults, the I_{SC} of the 4×4 PV sub-arrays is reduced by $I_{SC}/4$, $I_{SC}/3$, and $I_{SC}/2$ times when one, two, and three strings are open-circuited, respectively.
- In the shaded sub-array, the voltage at which the MPP settles ($V_{RPP-array}$) is always higher than the voltages ($V_{LL-array}$ and V_{UNF}) of the sub-array under fault and normal conditions.
- Interestingly, the MPP data of a PV sub-array with a duty cycle of 0.1 exhibits the same voltage for normal operation, OC faults, and PS events, except for LL and LG faults.

These observations provide valuable insights into the characteristics and behavior of different fault conditions in the PV system.

III. FAULT RATIO DETERMINATION

The MPP tracking process for LL/LG and OC faults is influenced by the location of the faults, resulting in distinct MPP tracking data associated with each fault type. These faults introduce notable changes in the MPP voltage and current of the affected sub-arrays. This paper leverages these variations to develop real-time fault ratios that enable the discrimination between normal and faulty sub-arrays. Specifically, a voltage-fault ratio (VFR) is formulated to detect LL/LG fault occurrences, while a current-fault ratio (CFR) is established to identify OC fault incidents.

A. Voltage-fault Ratio

To formulate the VFR, the data of the probable MPP voltage $V_{sPV,i-MPP}$ for i^{th} sub-array are extracted under the LL/LG fault conditions where single and multiple modules are grounded, as shown in Fig. 4(a). The data extraction is conducted for a large range of irradiation varying between 400 W/m^2 and 1000 W/m^2 , thereby ensuring the wide applicability of the VFR in practice. Fig. 4(a) also represents the MPP voltage $V_{MPP-global}$ under the normal operating condition to clarify the voltage reductions due to the faults, which is consistent with the discussion in Section II-B. To determine the LL/LG fault occurrence in a PV system, the VFR is then formulated as:

$$V_{f-ratio} = \frac{V_{sPV,i-MPP}}{V_{MPP-global}} \text{ for } i=1, 2, \dots, k \quad (1)$$

Fig. 4(b) shows the estimates of the VFR under the condition of the LL/LG fault occurrences in a 4×4 PV sub-array. Note that the VFR is estimated by considering all the possible LL/LG faults in the PV arrangement. With a handful of data considered for all the possible LL/LG faults incurred between 400 W/m^2 and 1000 W/m^2 , the maximum VFR for

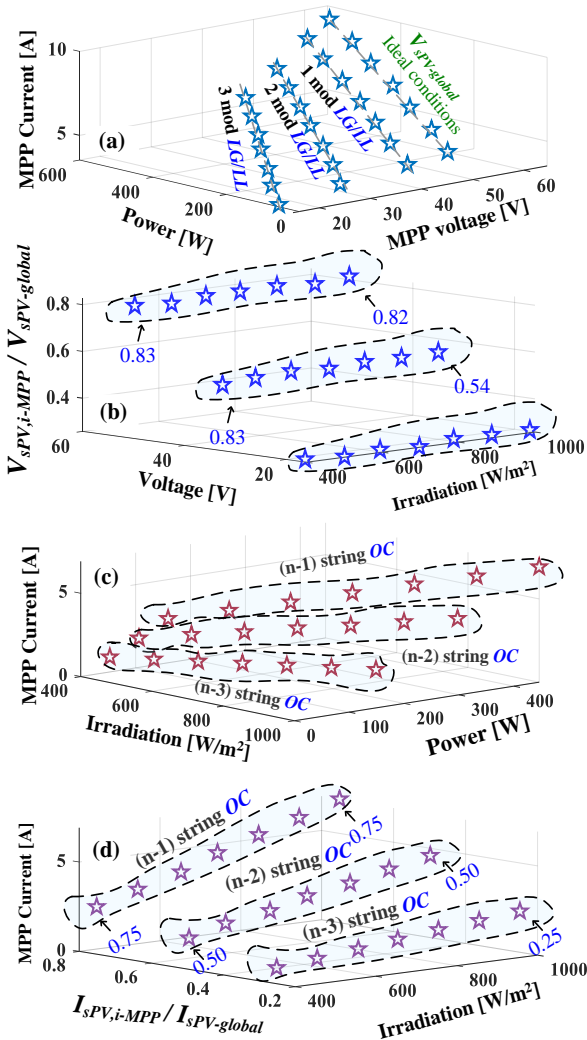


Fig. 4. (a) V , I , and P data and (b) fault ratio for the LL/LG fault, (c) G , I , and P data and (d) fault ratio for the OC faults.

one or more modules with the LL/LG faults is found to be $V_{f-ratio} = 0.83$. Importantly, this fault ratio is almost constant for all types of one-module LL/LG fault for a wide range of irradiation (i.e., from 400 W/m² to 1000 W/m²), which is a notable inference for this research work. Similarly, the VFRs for two- and three-module faults are found as 0.53 and 0.26 respectively. This confirms that the minimum possibility of a PV sub-array to experience the LL/LG fault is 0.83 and, consequently, that any other ratio below 0.83 will be estimated for the cases of two- and three-module faults in the PV sub-array. In other words, the equation to determine fault conditions in a PV arrangement is given as:

$$V_{f-ratio} = \frac{V_{sPV,i-MPP}}{V_{MPP-global}} < 0.83 \quad (2)$$

Since the VFR determination for a 4×4 PV sub-array is made only based on the MPP operating data extracted under its normal and fault conditions, the fault ratio is found to be valid for any $m \times n$ PV array.

Another question can arise that the MPP-tracked voltage (close to V_{oc} for the P&O algorithm) of the partially shaded PV sub-array will only reach the RPP (i.e., $V_{sPV-RPP}$) and hence it will always be $V_{MPP-global}$ if a shade is encountered. To explain the fault ratio determination in this case, the shade characteristic shown in Fig. 3(d) is considered. From the shaded PV array characteristics, the RPP voltages of two shade events are found to be 69.5 V and 75.0 V, whereas the normally operated (i.e., the uniformly irradiated) PV array voltage is realized as 64.5 V. This implies that the VFR determination is separately performed considering both probable shade events. In the first case, $V_{MPP-global}$ is assumed as 75.0 V, leading the fault ratio to be determined as 0.86 and for the second case as 69.5 V. It results in a fault ratio of 0.91. Thus, in either of the shade events, the VFR is greater than 0.83, and therefore, it is concluded that selecting the RPP voltage of the shaded PV array as $V_{sPV-global}$ has no harm in discriminating the PS event against the LL/LG faults.

B. Current-fault Ratio

Similar to the VFR, the CFR is a mandatory requirement to determine the occurrence of the OC faults in a PV sub-array. For this analysis, the same 4 × 4 PV array is considered and its MPP data (i.e., current, irradiation, and power) during the OC faults are represented in Fig. 4(c). Having the total $l = 4$ strings in a PV sub-array, the MPP data operated in ($l-1$), ($l-2$), and ($l-3$) strings at the OC fault condition is plotted for wide varying irradiation between 400 W/m² and 1000 W/m². MPP data are used to calculate the CFR of a PV arrangement:

$$I_{f-ratio} = \frac{I_{sPV,i-MPP}}{I_{MPP-global}} \text{ for } i=1, 2, \dots, k \quad (3)$$

$$I_{MPP-global} \gg I_{sPV,i-MPP} \quad (4)$$

where $I_{MPP-global}$ is the sub-array current under the normal operating condition and $I_{sPV,i-MPP}$ is the sub-array current under faulty conditions. Note that $I_{MPP-global}$ is the highest MPP current benchmarked in the PV arrangement. As in the case of LL/LG faults, the CFR for all the possible OC faults, which are prone to occur in a 4×4 PV array, is calculated using (3), and plotted in Fig. 4(d). It represents that the OC faults are found to be consistent with the following ratios: $0.75 \times I_{MPP}$.

global, $0.5 \times I_{MPP-global}$, and $0.25 \times I_{MPP-global}$ for ($l-1$), ($l-2$) and ($l-3$) strings, respectively, of a sub-array at the OC fault condition. In other words, the generalized representation of (3) for the CFR calculation of an i^{th} sub-array is given as:

$$I_{f-ratio,i} = \frac{I_{sPV,i-MPP}}{I_{MPP-global}} = \frac{k}{k-i} I_{MPP-global} \text{ for } i=1, 2, \dots, k \quad (5)$$

In Section IV, the proposed VFR and CFR [i.e., (1)–(5)] are further validated and are effectively used to determine fault occurrence under MPP-operated conditions. Once these ratios are validated to be true, LED arrangements are turned ON. Subsequently, the MCB tripping is enabled to isolate the inverter from the high fault current.

IV. DATA ANALYSIS AND VALIDATION

Despite that the fault ratios determined in Section III remain valid to confirm the fault occurrence, it is also necessary to discriminate the permanent faults (i.e., LL/LG and OC) from the temporary PS events. Moreover, the actual characteristics of the PV sub-array should exhibit changes in the open-circuit voltage and short-circuit current to confirm the fault occurrence. Meanwhile, the fault ratios are based on the P&O MPP algorithm; however, there is no guarantee that the algorithm is being deployed. Hence, when the fault ratios are determined by any of the MPP controllers, the faulty sub-array is mandated to undergo a verification check to confirm the fault occurrence. Furthermore, to enhance rapid fault

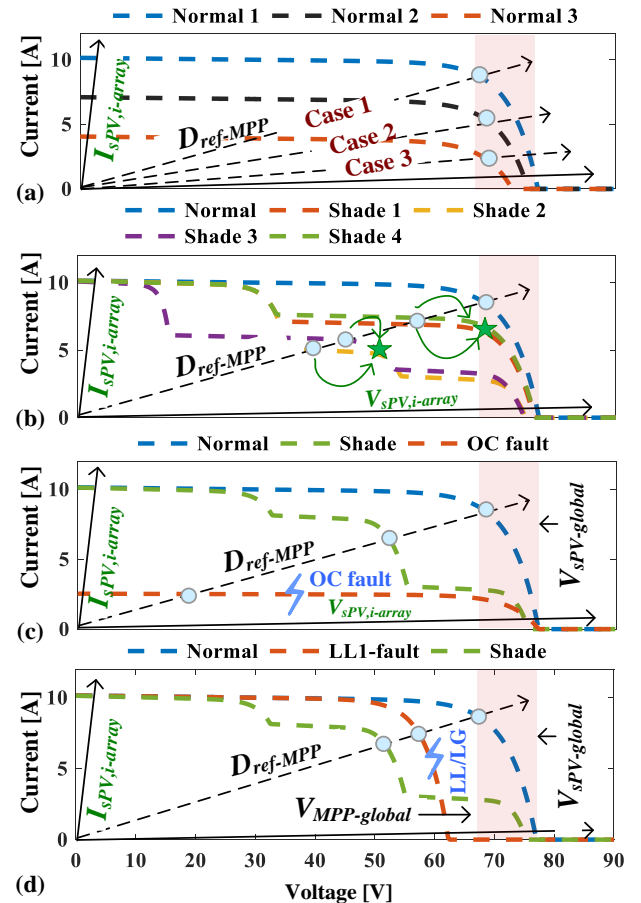


Fig. 5. I-V characteristic in comparison with the cases of (a) the uniform irradiation, (b) the PS event, (c) the OC fault, and (d) the LL/LG fault.

detection, the similarity of voltage and current as a function of V_{OC} and I_{SC} is presented in this section. The outcomes of this analysis are believed to possess the ability to accurately detect and discriminate the permanent faults (i.e., LL/LG and OC) from PS events, and also from the normal operating condition.

A. Observations at V_{OC} and I_{SC}

Having a detailed understanding of the I - V characteristics for the normal, PS event, and permanent fault conditions, it is found that the shaded PV sub-array exhibits many similarities with the sub-arrays under the normal condition and with the permanent faults.

To analyze the similarities with the normal case, Fig. 5(a) and 5(b) are presented that show the I - V characteristics for changes in the uniform (or ideal) irradiation and for the partial shading patterns. Similarly, Fig. 5(c) and 5(d) show the similarities of the shade event case along with the uniform irradiation case and against the permanent fault (i.e., LL/LG and OC) cases, respectively.

Since the fault behavior is streamlined to analyze the voltage and current samples at V_{OC} and I_{SC} , the load lines pertinent to the 10% duty and the 90% duty are marked in the I - V characteristic curves. From the load-line intersection, it is inferred that for both the permanent faults and temporary events, the voltage value at the 10% duty is always found at the constant voltage region (close to V_{OC}) and, similarly, the current at the 90% duty is found in the constant current region (close to I_{SC}). The representation of two former data points in the I - V characteristics is given as follows: (i) the sub-array voltage ($V_{sPV,i-array}$) in the constant voltage region and (ii) the sub-array current ($I_{sPV,i-array}$), as:

$$V \text{ at } 0.1 \text{ duty} = V_{sPV,i-array}, \text{ for } i=1,2,\dots,k, \quad (6)$$

$$I \text{ at } 0.9 \text{ duty} = I_{sPV,i-array}, \text{ for } i=1,2,\dots,k. \quad (7)$$

Detailed observation on the I - V characteristics plotted in Fig. 5 illustrates that the normal operation, the PS event, and the OC fault lead the range of V_{OC} to become similar with each other: i.e., the voltages differ only negligibly. Similarly, it is a notable inference that the range of I_{SC} remains the same for the normal and PS conditions. To discriminate the fault types, the sub-array to record the highest voltage and current at V_{OC} and I_{SC} are denoted as $V_{sPV-global}$ and $I_{sPV-global}$, respectively.

B. Discriminating the Normal Operation and the PS Event

The PS events recognized by multiple steps in the I - V characteristic curves are temporary; however, it is still possible for the PS events to accompany the permanent faults (i.e., LL/LG and OC). It implies that the PS events should be discriminated as the first abnormal condition in the detection process. In this paper, it is achieved using the three-sample procedure.

Specifically, unlike the case of the conventional MPP tracking, the MPP zone of the PV sub-array is estimated by using its voltage and current samples: i.e., $V_{sPV,i-array}$ and $I_{sPV,i-array}$. Moreover, the MPP resistance $R_{MPP,i}$ of the i^{th} sub-array and the corresponding duty value $D_{ref-MPP,i}$ of the DC-DC converter is estimated as:

$$R_{MPP,i} = \left(V_{sPV,i-array} / I_{sPV,i-array} \right), \text{ for } i=1,2,\dots,k, \quad (8)$$

$$D_{ref-MPP,i} = 1 - \sqrt{(R_{MPP,i} / R_L)} \quad (9)$$

where R_L is the fixed resistance. Having the reference duty in (9), the P&O algorithm is then declared with $D_{ref-MPP,i}$ to locate the first immediate power peak in the I - V characteristics. This peak is marked as the actual MPP with the dataset of $(V_{sPV,i-MPP}, I_{sPV,i-MPP})$. For instance, the I - V characteristics of a normal sub-array with three uniform irradiation changes is considered as shown in Fig. 5(a).

With the reference data from $V_{sPV,i-array}$ and $I_{sPV,i-array}$, $D_{ref-MPP,i}$ for the three various irradiation changes is estimated by (9) and the P&O MPP tracking is then initiated. The MPP dataset [i.e., $(V_{sPV,i-MPP}, I_{sPV,i-MPP})$] obtained by the duty reference are found in relation with $(V_{sPV,i-array}, I_{sPV,i-array})$, as:

$$V_{sPV,i-MPP} \geq 0.8V_{sPV,i-array}, \quad (10)$$

$$I_{sPV,i-MPP} \geq 0.9I_{sPV,i-array}, \quad (11)$$

Thus, (10) and (11) stand valid to estimate the MPP and determine the dataset of $(V_{sPV,i-MPP}, I_{sPV,i-MPP})$. It enables the indication to estimate the maximum available power of a sub-array. Moreover, (10) and (11) are verified with the values of the MPP data presented for the case of uniform irradiation, shown in Fig. 5(a).

Given the MPP data of three various irradiances, the maximum MPP voltage ($V_{MPP-global}$) and current ($I_{MPP-global}$) of the multiple PV sub-arrays are determined. To confirm the occurrence of the uniformly irradiated condition, the reference MPP voltage and current estimated based on (10) and (11) are referred as $V_{sPV,i-MPP-ref} = 0.8V_{sPV,i-array}$ and $I_{sPV,i-MPP-ref} = 0.9I_{sPV,i-array}$.

To understand the shade occurrence in a PV sub-array, four various shade events are plotted along with uniform irradiated cases in Fig. 5(b). From the characteristics, for both the uniformly irradiated event and the partial shading event, the datasets of $(V_{sPV,i-array}, I_{sPV,i-array})$ at the 0.1 and 0.9 duty ratios are identified to have negligible differences. Furthermore, for the normally irradiated condition, the approximated MPP load line reference ($R_{MPP,i}$) settles the P&O algorithm to the first immediate MPP data, which follows the relations in (10) and (11). This confirms the validations with (10) and (11) are true, whereas the same load line for the PS events has always been located at the operating point that is not in agreement with the uniformly irradiated cases. For identification, the probable settling point of the P&O algorithm declared from D_{ref} (i.e., 0.1) to reach $D_{ref-MPP,i}$, is marked using a green arrow in Fig. 5(b).

In addition, the discrimination between the PS event and the uniform, time-varying irradiation case can be achieved by establishing the mathematical relationship between the actual and estimated data as:

$$\text{Normal: } \begin{cases} V_{sPV,i-MPP,ref} \geq V_{sPV,i-MPP} \\ I_{sPV,i-MPP,ref} \geq I_{sPV,i-MPP} \end{cases}, \quad (12)$$

$$\text{Shading: otherwise.}$$

Thus, the PS events can be discriminated from the normal operation by having the reference data point of the PV array at V_{OC} , I_{SC} , and $D_{ref-MPP}$. The proposed shade detection procedure can be converged rapidly with short switching transients.

C. Locating the LL, LG, and OC Faults

Fig. 5(c) and 5(d) present the effects of the LL/LG and OC faults on the normal and shaded I - V characteristics. Note that the LL/LG characteristic for the one-module-grounded condition is preferred, because the voltage mismatch at V_{OC} records the least difference between the normal and fault characteristics. Any other LL/LG fault in the 4×4 PV sub-array is verified to produce a higher voltage difference at V_{OC} than the former. For the OC fault, three strings in the 4×4 PV array are excluded and hence, $I_{sPV,i-array}$ is reduced to $I_{sPV,-global} / 3$. Having studied the I - V characteristic of the permanent faults (i.e., LL/LG and OC) as a function of the 0.1 duty and the 0.9 duty (i.e., $V_{sPV,array}$, $I_{sPV,array}$), the significant inferences to discriminate the permanent fault cases from the normal and non-permanent (i.e., shade) cases are listed as follows.

- For the non-permanent cases, $V_{sPV,array}$ is always found to lie in the range of ΔV and its limit is presented in (13). For instance, the $V_{sPV,array}$ values of the shaded and normal cases have a similar voltage range, whereas the LL/LG fault case with the least module mismatch has encountered a higher voltage difference. Given the actual $V_{MPP-global}$ value tracked by the P&O algorithm, it confirms that any LL/LG fault will not always lie between $V_{MPP-global}$ and $V_{sPV-global}$. Note that any LL/LG fault with a higher level of mismatch is obvious to record less $V_{sPV,array}$ than the former, which is also confirmed by (13):

$$\Delta V = V_{MPP-global} \sim V_{sPV-global} \cdot \quad (13)$$

If none of the PV sub-array is verified with the uniformly irradiated condition, $V_{MPP-global}$ is then replaced by $V_{sPV,i-MPP-ref}$ estimated from $V_{sPV-global}$.

- For the minimal probable LL/LG fault, $V_{sPV,array}$ is found to be less than $V_{MPP-global}$. In other words, it represents $V_{sPV,array} \neq \Delta V$.
- With l columns in a PV sub-array, $I_{OC-fault,i}$ is reduced to $I_{sPV-global} / (l-1)$, $I_{sPV-global} / (l-2)$, and $I_{sPV-global} / (l-(l-1))$ for $(l-1)$, $(l-2)$, and $(l-(l-1))$ strings open-circuited in the i^{th} PV sub-array. Then, (14) can be used to identify the OC fault in a PV sub-array,

$$I_{OC-fault,i} = \frac{k}{k-i} I_{sPV-global} \approx \frac{k}{k-i}, \text{ for } i = 1, 2, \dots, k \quad (14)$$

Following the discrimination (i.e., the normal and shade cases) discussed in the earlier section, the permanent faults in a sub-array of a PV arrangement are proven to be identified based on the two reference data points $V_{sPV,array}$ and $I_{sPV,array}$ (or, equivalently, the data points at V_{OC} and I_{SC}).

D. Fault Detector-Array Combiner Box (FD-ACB)

During normal operations, the VFR and CFR are continuously monitored, and if an abnormality is found, the MCB is immediately tripped to protect the inverter from abnormality. Furthermore, the FD-ACB switching is

TABLE II
SWITCHING PATTERNS TO DETERMINE THE FAULT OCCURRENCE
IN PV SUB-ARRAYS.

Test case	S_{L1}	S_{L2}	S_{L3}	S_{PV1}	S_{PV2}	S_{PV3}	Load	MCB	CV
Fault in SA-1				✓			R-load	-	D_1
Fault in SA-2					✓		R-load	-	D_2
Fault in SA-3						✓	R-load	-	D_3
Normal case	✓	✓	✓				Inverter	✓	D_1, D_2, D_3

Sub-Array – SA, Control Variables -CV

necessitated to discriminate the nature of PV fault. This FD-ACB switching enables faster maintenance because the fault type is discriminated within three samples. Three triggering samples from each sub-array, which are required from the sub-array, are: (i) voltage at the constant voltage regions ($V_{sPV,array}$), (ii) current at the constant current regions ($I_{sPV,array}$), and (iii) the actual MPP data of the PV sub-array ($D_{ref-MPP}$, $V_{sPV,i-MPP}$, $I_{sPV,i-MPP}$). To obtain these datasets, a dedicated trial run is conducted for each PV sub-array. To facilitate the collection of sub-array data for fault discrimination, a novel FD-ACB is introduced in this paper.

Under the normal operating condition, all the sub-array switches (i.e., S_{PV1} , S_{PV2} , ..., S_{PVn} in Fig. 1) are turned on to connect with the main DC rail. On the other hand, to identify the fault conditions of the PV sub-array, the array switches are turned off and the line switches (i.e., S_{L1} , S_{L2} , ..., S_{Ln} in Fig. 1) of the PV sub-arrays are sequentially turned on to determine the fault occurrence. Table II represents the switching patterns followed to determine the voltage, current, and MPP samples of the sub-arrays. Note that the sub-arrays are found to be electronically disconnected from the main DC rail to get the actual status (i.e., the faulty/normal operating conditions) of the PV sub-arrays. This arrangement can readily be extended to micro-inverters and string-level converters, enabling wide application of the proposed fault detection and discrimination method.

E. Flowchart

Fig. 6 shows the flowchart of the proposed MPP-based method, which summarizes the tasks discussed in Sections II–IV, as follows.

- Step 1** (PV arrangement data): getting the total number of PV sub-arrays k and the numbers of rows m and columns n in each sub-array;
- Step 2** (MPP data of PV sub-array): determining the MPP data (i.e., $V_{sPV,i-MPP}$ and $I_{sPV,i-MPP}$ for $i = 1, 2, \dots, k$) of all the PV sub-arrays;
- Step 3** (Criterion to locate irradiation change): Rapid or fast irradiation changes (IC) are detected based on the voltage and current references monitored between iterations. The equations to determine IC is given in (15) and (16):

$$\frac{V_{PV}(x) - V_{PV}(x-1)}{V_{PV}(x)} \geq 0.2, \quad (15)$$

$$\frac{I_{PV}(x) - I_{PV}(x-1)}{I_{PV}(x)} \geq 0.1, \quad (16)$$

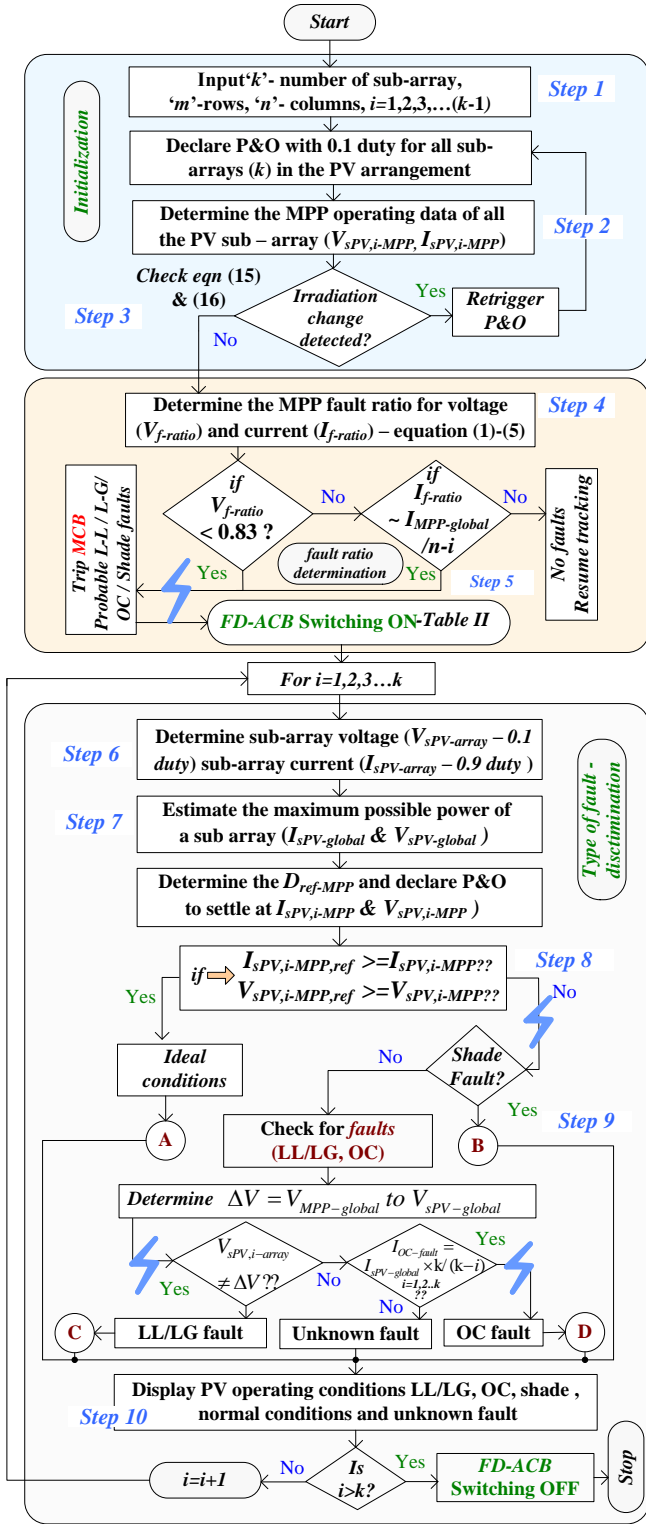


Fig. 6. Flowchart - PV fault detection and discrimination.

where ‘x’ denotes iteration number, V_{PV} and I_{PV} are the voltage and current values of the sub-array. Note that the ratios for the latter equations are verified and updated based on the existing literature [30].

Step 4 (fault ratio determination): given the MPP data, estimate $V_{sPV-global}$ and $I_{sPV-global}$ to identify $V_{f-ratio}$ and $I_{f-ratio}$ for the i^{th} sub-array;

- Step 5** (Criterion to turn FD-ACB on): turning on the FD-ACB to locate the faulty sub-array, based on (2) and (5) with $V_{f-ratio}$ and $I_{f-ratio}$, respectively, and Table II;
- Step 6** (FD-ACB switching): performing the sub-array switching, based on Table II, to determine the sub-array voltage at the 0.1 duty (i.e., $V_{sPV,i-array}$), the sub-array current at the 0.9 duty (i.e., $I_{sPV,i-array}$), and the actual MPP data pertinent to $D_{ref-MPP}$;
- Step 7** (PV sub-array estimated data): benchmarking the global best array data (i.e., $V_{sPV-global}$ and $I_{sPV-global}$) for each sub-array and estimating the global best data (i.e., $V_{MPP-global}$ and $I_{MPP-global}$) among PV sub-arrays, based on (10) and (11);
- Step 8** (Discriminating ideal cases): discriminating the normally operating case from temporary and permanent faults by evaluating the actual and reference MPP data, based on (12);
- Step 9** (Determining ΔV and $I_{OC-fault,i}$): calculating the limit of ΔV to locate the LL and LG faults and the current ratio (i.e., $I_{OC-fault,i}$) to locate the OC fault, given the data extracted from the PV sub-array during the FD-ACB switching;
- Step 10** (Determining fault type): Various operating conditions like LL/LG, OC, PS and normal conditions are identified. Thereby the LED is continued to be turned ON, such that the fault status of the PV sub-array is indicated.

V. TEST SETUP AND CASE STUDY RESULTS

The modeling of the PV system was carried out using MATLAB /SIMULINK on a high-performance PC equipped with an Intel i7 processor, 32 GB RAM, and a 2 TB HDD. The PV modeling utilized the data from shell S36, and the specific values from its datasheet can be found in Table III. To verify the fault ratios, a series of case studies were conducted, and once the occurrence of a fault was confirmed, the FD-ACB switching was initiated to identify the fault type. Both simulation and hardware verification were employed to ensure accurate determination of fault occurrences.

Simulation verifications were performed using the MATLAB/SIMULINK model. Also, a laboratory-scale prototype model was constructed for hardware verification of the fault ratios. The prototype model consisted of a 12 kW *itech* PV simulator, a DC-DC converter, LEM sensors, an Arduino UNO controller, and a designated ‘R’ load. The designed lab-scale prototype model is presented in Fig.7. To conduct experiments, the I-V characteristics under normal, shade, and fault conditions were programmed into the PV simulator, and the conventional P&O algorithm was employed to track the MPP. Detailed design parameters of the DC-DC converter can be found in Table IV. The case studies encompassed both temporary and permanent abnormal events, and the results of each case study were comprehensively analyzed.

A. Case Study 1: LG and Shade Faults

In Case Study 1, Sub-array 1 was programmed with the LG fault, Sub-array 2 with normal operating conditions, and Sub-array 3 with shaded conditions, as illustrated in Fig. 8. To evaluate the effects of the faults, the I-V characteristics of all three sub-arrays were simulated and presented in Fig. 9(a).

TABLE III
SHELL S36 DATASET

No	Parameters	Values
1	Power at the MPP P_{mpp}	36 W
2	MPP voltage V_{mpp}	16.5 V
3	MPP Current I_{mpp}	2.05 A
4	Open circuit voltage V_{oc}	21.4 V
5	Short circuit current I_{sc}	2.30 A

TABLE IV
DESIGN SPECIFICATION OF DC-DC BOOST CONVERTER

Shell S36 Panel details		
1	Power at MPP P_{mpp}	36W
2	Power voltage V_{mpp}	16.5V
3	Open circuit voltage V_{oc}	21.4V
4	Short circuit current I_{sc}	2.30A

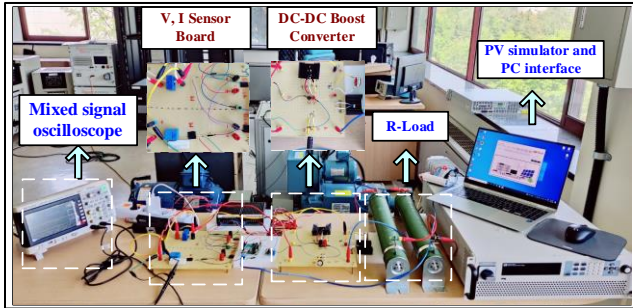


Fig.7. Hardware prototype model

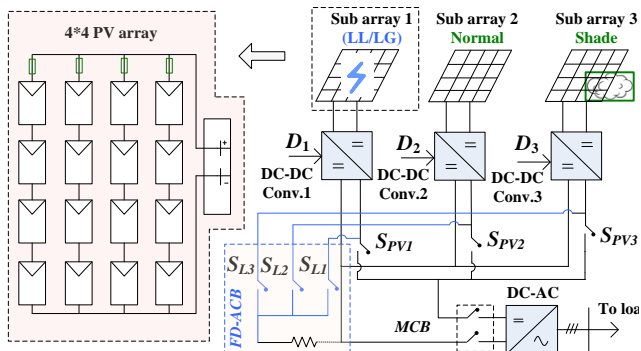


Fig. 8. Test setup with the LG and shade faults.

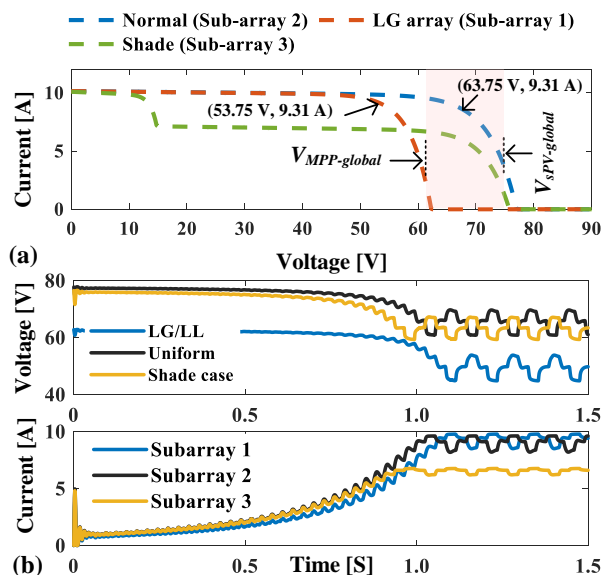


Fig. 9. (a) I - V characteristics of Sub-arrays 1-3 and (b) the convergence characteristics of Sub-arrays 1-3 for the LG and shade faults.

The I - V characteristics of Sub-arrays 2 and 3 exhibited a similar voltage range, with a negligible voltage difference denoted as $\Delta V_{sPV2-array} \approx \Delta V_{sPV3-array} \approx \Delta V$. However, Sub-array 1 displayed a significant voltage difference compared to the other sub-arrays (i.e., Sub-arrays 2 and 3). By referring to the sub-array voltages, the global maximum voltage at V_{OC} was identified as $V_{sPV-global} = 77.91$ V. The corresponding reference for the MPP was estimated as $V_{sPV-MPP,ref} = 63.75$ V.

i. Fault Ratio Verification: Case Study 1

To evaluate the faulty conditions in the PV arrangement, the sub-arrays were implemented with the P&O algorithm at the 0.1 duty (i.e., at constant voltage regions) to track the MPP. Owing to the duty declaration, the voltage and current convergences of all the PV sub-array are presented as shown in Fig. 9(b). Acknowledging the circuitual changes made by the LG fault and shade event, Sub-array 1 tracked the MPP value of 52.82 V and 9.77 A. Similarly, Sub-arrays 2 and 3 tracked the values of (69.43 V, 9.03 A) and (64.40 V, 6.21 A), respectively. The P&O algorithm for the MPP tracking and settlement at the three reference points are referred to in [30]. Among the multiple MPP voltages, the global best MPP reference was obtained as $V_{MPP-global} = 69.43$ V for Sub-array

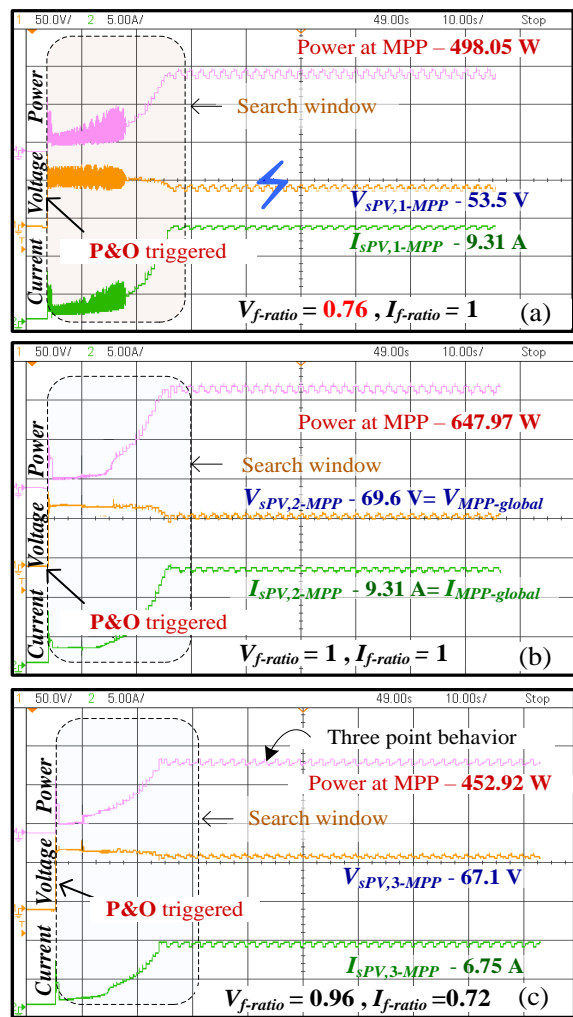


Fig.10. Fault ratio verification for Case Study 1: (a) LG fault, (b) Normal and (c) shade cases.

2. For Sub-arrays 1, 2, and 3, $V_{f-ratio}$ were estimated as 0.76, 1.00 and 0.96, respectively, and $I_{f-ratio}$ were identified as 0.96, 1.02 and 0.72, respectively.

Fig. 10. presents the hardware verification of sub-array in LG, normal and PSC events. Programmed with the LG fault, the hardware design introducing plenty of oscillations is clearly visible in Fig. 10(a). However, the normal and shade operating conditions in Fig. 10(b) and 10(c) remain to produce clear waveforms with the typical three-point behavior after reaching convergence. Despite sharing the common DC voltage in the DC link, the fault ratios are crucial in determining the faults in the sub-arrays, the proposed fault ratios in (1)-(5) are served to detect the abnormality in these cases. Programmed with various operating conditions, Sub-array 1 has benchmarked 53.5 V as $V_{SPV,1-MPP}$, and the remaining in normal and shade cases benchmark 69.6V and 67.1 V as $V_{SPV,2-MPP}$ and $V_{SPV,3-MPP}$. The hardware realization also illustrates the MPP of sub-array's $I_{SPV,1-MPP}$, $I_{SPV,2-MPP}$ and $I_{SPV,3-MPP}$ settling to 9.31 A, 9.31 A, and 6.75 A respectively. Verification of fault ratios confirms the appearance of LL/LG fault in Sub-array 1. Since the VFR of Sub-array 1 fell below 0.83, the probability of the permanent LG fault was manifested and, hence, the FD-ACB switching was initiated to verify the voltage range ΔV (69.43 V to 77.91 V). The FD-ACB switching to connect the sub-arrays to the R-load was made by referring to Table II.

ii. FD-ACB Verification: Case Study 1

The case study results of the FD-ACB switching for Sub-arrays 1–3 is presented in Fig. 11. Tracking data of various sub-arrays are exported to the Excel sheet, and real-time verification is performed in MATLAB/SIMULINK. Note that FD-ACB switching requires real-time data, which demands a high-cost DAQ (data acquisition) to record three various sub-array data. To appreciate simple and less costly experimentation, the authors have recorded the real-time data from hardware experiments and, subsequently, the SIMULINK verification with FD-ACB switching is conducted for verifying the fault nature. Despite the limitation with DAQ, the FD-ACB experimentation is very novel, mathematically valid, and judicial to discriminate the fault nature.

For the identification, $V_{f-ratio}$, $I_{f-ratio}$, $V_{SPV-array}$, $I_{SPV-array}$, and V_{LED} were recorded and plotted for all the sub-arrays. To determine the occurrence of a fault, the LED voltage was switched to 0.70 V from 0 V, when the permanent fault conditions were encountered. From Fig. 11, it is noted that the sequential switching in FD-ACB was made and the three reference points of the PV sub-array were determined respectively to confirm the fault occurrence. Note that the P&O was declared from the third reference data sample and once it was settled, the next sub-array in the sequence was switched to identify the changes with V_{OC} and I_{SC} . It is important to note here that the PV sub-array failing to fall in the ΔV range was declared in the fault condition and its corresponding LED was turned on. From the MPP operation, the ΔV range of the PV arrangement was found as 67.91 V to 77.91 V. On evaluations with the FD-ACB switching and its MPP datasets, Sub-array 1 with $V_{SPV,1-array} = 62.87$ V was diagnosed with the permanent LG fault due to $V_{SPV,i-array} \neq \Delta V$

and Sub-array 3 was determined with the temporary shade faults. Thus, the proposed method using the FD-ACB was found successful to detect, discriminate, and locate the PV faults.

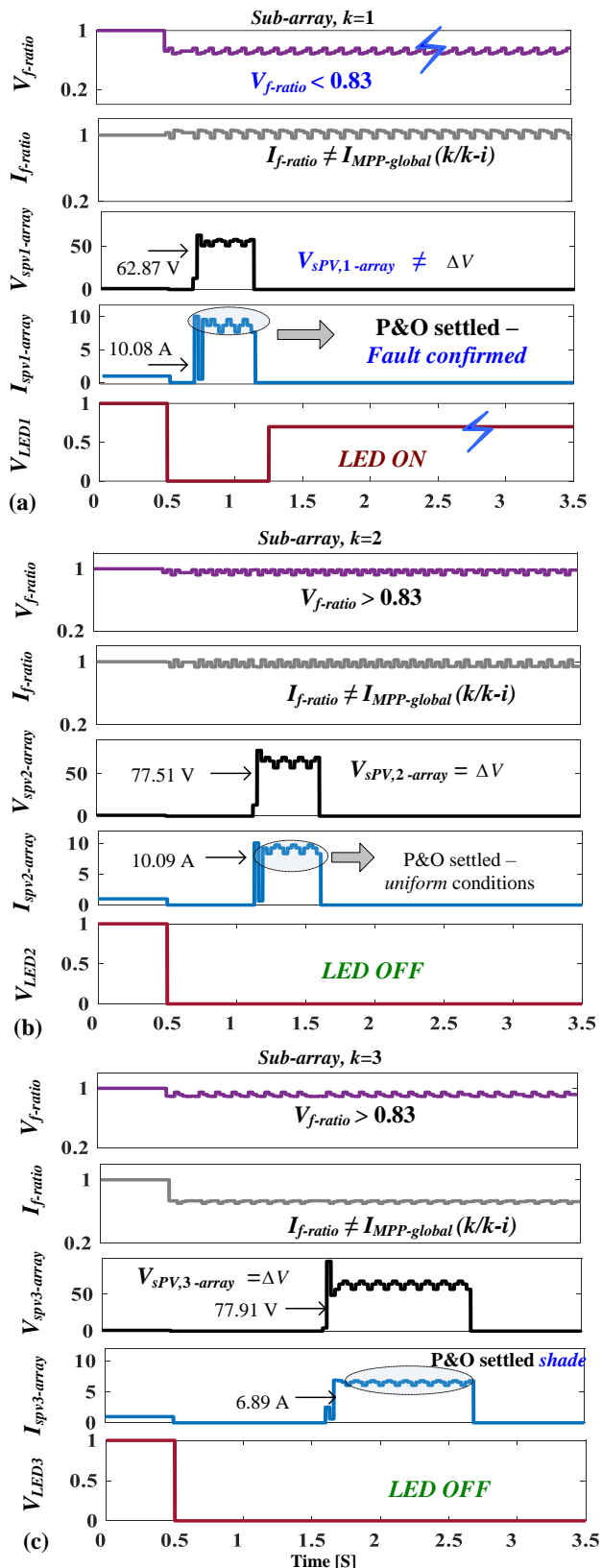


Fig. 11. Results of the PV system operation and FD-ACB switching for the LG and shade faults: (a), (b), (c) Sub-arrays 1, 2 and 3.

B. Case Study 2: LL and OC Faults

For Case Study 2, Fig. 12 illustrates the programming of specific faults for each sub-array. The permanent LL fault was programmed to Sub-array 2, the OC fault to Sub-array 3, and the normal operating condition to Sub-array 1. As a result of these programmed faults, a significant disparity in the voltage and current values at the MPP was observed, as depicted in Fig. 13(a). Furthermore, during the evaluation of the PV sub-array, $V_{MPP-global}$ (the global maximum power point voltage) and $V_{sPV-global}$ were identified as 69.41 V and 77.03 V, respectively. The corresponding range value was determined to distinguish between temporary and permanent faults within the sub-array.

i. Fault Ratio Verification: Case study 2

Fig. 13(b) shows the simulated results for voltage and current convergences of the MPP tracking for Sub-arrays 1–3. It is clear that the MPP-tracked voltage of Sub-array 2 had a significant drop to 21.05 V due to the LL fault. Similarly, Sub-array 3 programmed with the OC fault also acknowledged the monumental difference in the MPP current (i.e., 2.30 A) to suspect the occurrence of the permanent fault. Among the three sub-arrays, the PV sub-array under the normal operating

condition (i.e., Sub-array 1) recorded the highest value of 69.43 V as $V_{MPP-global}$, and Sub-arrays 2 and 3 recorded 19.04 V and 67.15 V, respectively. On calculations to VFR, Sub-arrays 1–3 recorded the values of 1, 0.25 and 0.94, respectively, as $V_f-ratio$, confirming the LL fault in Sub-array 2. On the other hand, the CFRs (i.e., $I_f-ratio$) of Sub-arrays 1–3 were estimated as 0.99, 1.03, and 0.25, respectively. Since $I_f-ratio$ of the sub-array lay in the range shown in (5), the quest of the OC fault occurrence was raised and hence the FD-ACB switching was mandated. After the simulated verification indicated the occurrence of faults in Sub-arrays 2 and 3, further hardware verification was conducted to confirm the presence of PV faults. Fig. 14 illustrates the hardware verification process and the confirmation of fault ratios for Sub-array 1-3 in case study 2.

With uniform or normal conditions programmed in Sub-array 1, the values of $V_{sPV,1-MPP}$ and $I_{sPV,1-MPP}$ were determined to be 69.6 V and 9.31 A, respectively. It is important to note that these MPP values for Sub-array 1 were also used as benchmarks for $V_{MPP-global}$ and $I_{MPP-global}$, because the uniform conditions were identified and verified. Experimental verification for Sub-array 2 yielded the values of 19.3 V and 9.42 A for $V_{sPV,2-MPP}$ and $I_{sPV,2-MPP}$ respectively, indicating the

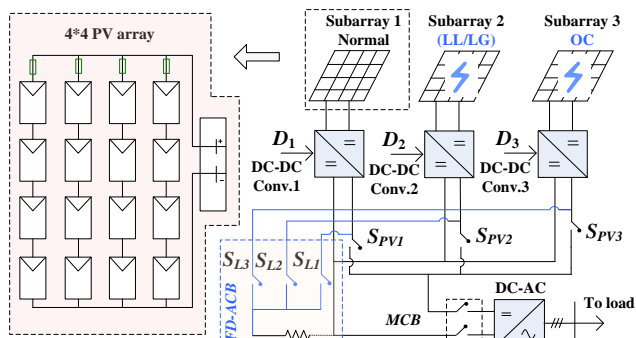


Fig. 12. Test setup with the LL and OC faults.

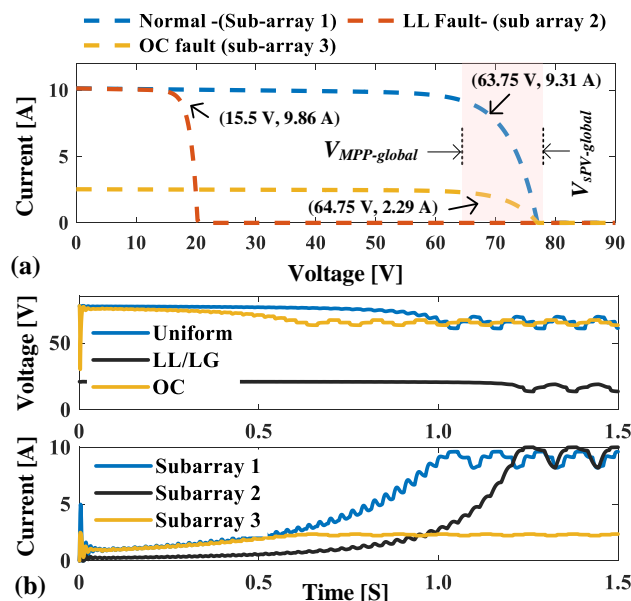


Fig. 13. I-V characteristics of Sub-arrays 1-3 and (b) the convergence characteristics of Sub-arrays 1-3 for the LL and OC faults.

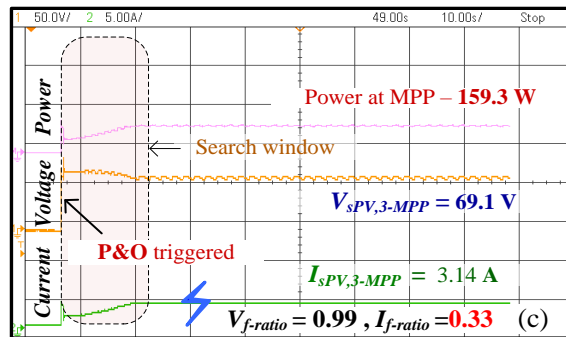
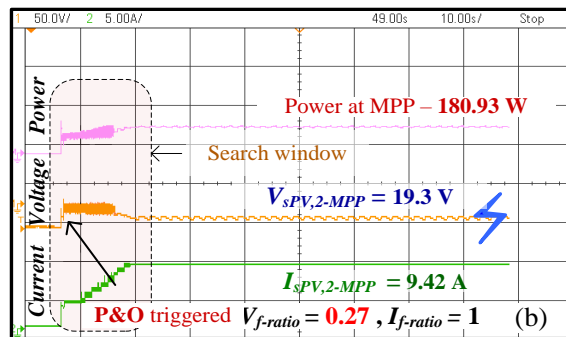
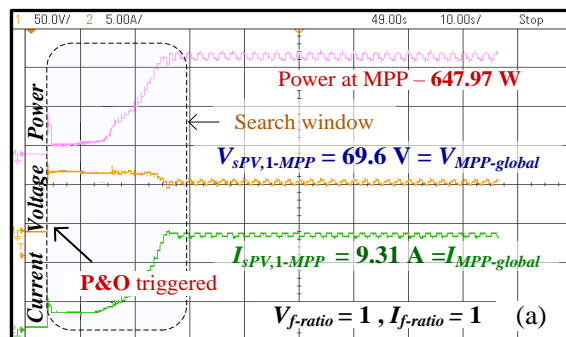


Fig. 14. Fault ratio verification for Case Study 2: (a) normal conditions, (b) LL fault and (c) OC fault.

occurrence of an LL fault. Similarly, for Sub-array 3, the values of 69.1 V and 3.14 A were obtained for $V_{sPV,3-MPP}$ and $I_{sPV,3-MPP}$, confirming the presence of a fault. The calculated values of VFR were 1, 0.27, and 0.99 for Sub-array 1, 2, and 3 respectively, further supporting the identification of the LL fault in Sub-array 2. Additionally, the CFR values were determined as 1, 1, and 0.33 for Sub-arrays 1, 2, and 3 respectively, verifying the occurrence of the fault in Sub-array 3. Upon confirming the fault occurrence in Sub-arrays 2 and 3, the MCB connected to the inverter tripped. Subsequently, the FD-ACB switching was evaluated to determine the type of fault.

ii. *FD-ACB Verification: Case Study 2*

To confirm the occurrence of the PV faults, the FD-ACB switching was performed, and its changes in the characteristics of V_{OC} and I_{SC} were analyzed as shown in Fig. 15. Having reference from Table II, the sub-array testing was performed and its parameters such as $V_{sPV-array}$, $I_{sPV-array}$ and V_{LED} were recorded. For reference, $V_{f-ratio}$ and $I_{f-ratio}$ of all the sub-arrays were also recorded with suspicion of the faults in Sub-arrays 2 and 3. Having ΔV (i.e., from 69.43 V to 77.51 V) and I_{SC} of Sub-arrays 1–3, the LL fault was manifested in the PV arrangement. First, Sub-array 1 recorded 77.51 V and 10.09 A as $V_{sPV-array}$ and $I_{sPV-array}$, respectively, implying that it operated under normal operating condition. However, Sub-array 2 was determined to have 21.05 V as $V_{sPV-array}$ and 10.04 A as $I_{sPV-array}$, confirming the LL fault. For the case of Sub-array 3, 76.36 V and 2.53 A were recorded as $V_{sPV-array}$ and $I_{sPV-array}$, verifying the OC fault occurrence. Having the faults confirmed in Sub-arrays 2 and 3, the corresponding LEDs were turned on. This demonstrated that the proposed method was effective in detecting, discriminating, and identifying the temporary (shade) and permanent (LL/LG, OC) faults in the PV arrangement.

VI. COMPARATIVE DISCUSSION

For a comprehensive understanding of the proposed fault detection scheme, a thorough comparison is conducted, analyzing the sensor used, fault detection features, discrimination ability, exclusive remarks, and limitations. To achieve this, various methods in the literature are categorized into instrument-based methods (IBM), sensor-based methods (SBM), MPPT-based techniques (MBT), artificial intelligence-based techniques (AIT), and fault ratio-based methods (FBD). Additionally, these methods are compared with the proposed method, and the observations on various parameters are presented in Table V. This comparative study provides insights into the uniqueness and advantages of the proposed method over existing literature. Based on the comparison presented in Table V, the merits of the proposed method are explained with the following aspects:

- **Commercialization:** Commercialization plays a crucial role in enhancing safety in PV power generation. The proposed FD-ACB implementation, which shares a similar architecture with conventional PV systems, has significant potential for commercial PV inverters. Furthermore, the experimentation of the proposed method with multiple PV arrays is relatively novel in existing literature, greatly enhancing PV protection.

- **CAPEX Cost:** The capital expenditure encompasses various components such as sensors, wiring arrangements,

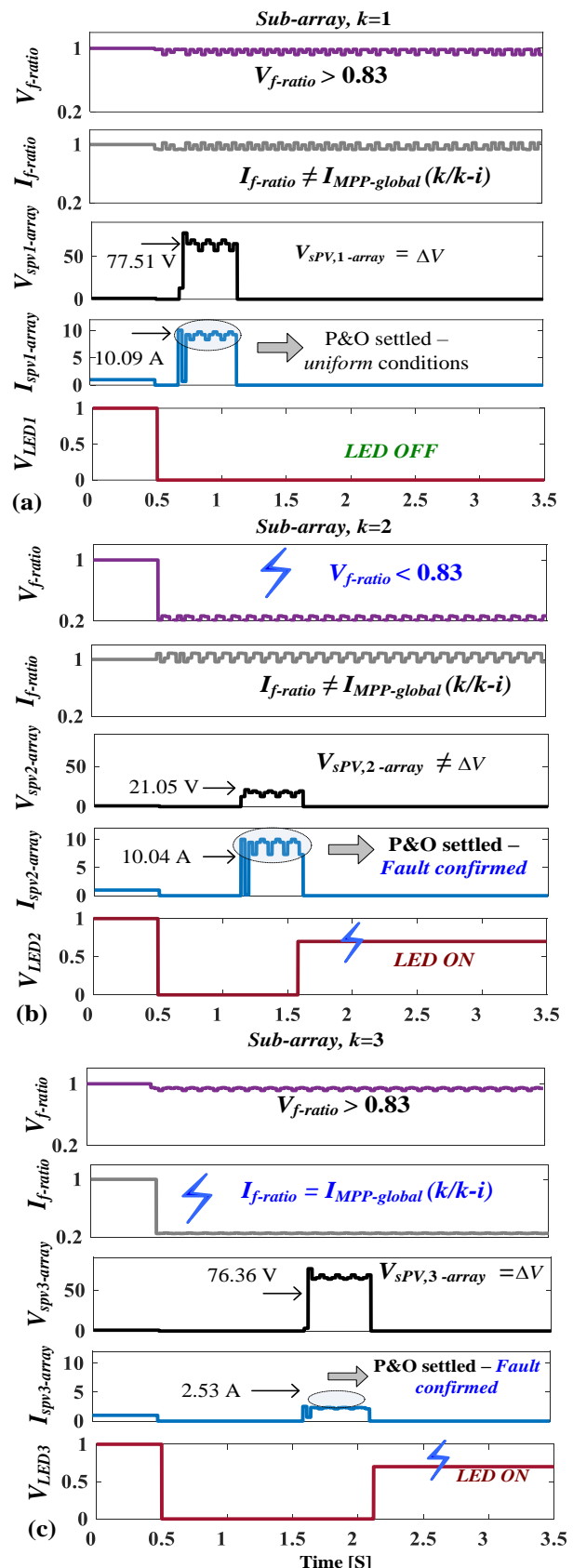


Fig. 15. Results of the PV system operation and FD-ACB switching for the LL and OC faults: (a), (b), (c) Sub-arrays 1, 2 and 3.

Table V
COMPARATIVE STUDY OF VARIOUS FAULT DETECTION METHODS WITH FD-ACB

Category	Ref	Array size	Instrument/Sensors	Features		Discriminated fault				Remarks	Limitations
				DET	DISC	LL	LG	OC	PSC		
IBM	[3]	2×1	Infrared sensor	✓	×	×	×	×	×	<ul style="list-style-type: none"> Faults can only be located after the temperature rise / hotspots. 	<ul style="list-style-type: none"> Additional instruments are a mandatory requirement.
	[4]	8×3	Device under test	✓	×	×	×	×	×	<ul style="list-style-type: none"> Only string level faults can be located. 	<ul style="list-style-type: none"> Fault categorization cannot be made to facilitate maintenance.
	[5]	1×1	Impedance Spectroscopy	✓	×	×	×	×	×	<ul style="list-style-type: none"> The measurement can only be applied to GaAs/Ge cell type. 	<ul style="list-style-type: none">
SBM	[6]	3×3	Voltage Sensor	✓	×	×	×	×	×	<ul style="list-style-type: none"> String level voltage sensors are employed to detect healthy string. 	<ul style="list-style-type: none"> Additional voltage, current sensors are needed.
	[7]	1×1	WPS	✓	×	×	×	×	×	<ul style="list-style-type: none"> Module level abnormality with voltage and current is monitored. 	<ul style="list-style-type: none"> Capital cost investment is excessively high for a higher PV array size.
	[8]	4×3	DC switch boards	✓	✓	✓	✓	×	×	<ul style="list-style-type: none"> Despite the comprehensive analysis on fault type, the results are uncertain to detect and discriminate various PV faults. 	<ul style="list-style-type: none"> Additional maintenance is needed for instruments.
	[9]	4×4	Voltage sensor	✓	✓	✓	✓	×	✓	<ul style="list-style-type: none"> Voltage sensors are placed per two strings to detect the permanent LL/LG faults. 	<ul style="list-style-type: none"> Maintenance is very high.
MBT	[15]	4×4	-	✓	✓	✓	✓	×	✓	<ul style="list-style-type: none"> A wavelet technique is incorporated to MPPT to detect PS, LL, and LG faults. 	<ul style="list-style-type: none"> MPP data are monitored, and mandatory to locate fault.
	[16]	5×3	-	✓	✓	✓	✓	×	✓	<ul style="list-style-type: none"> A RPP based voltage ratio is implemented to detect LL/LG and PS faults. 	<ul style="list-style-type: none"> Instantaneous discrimination cannot be made.
AIT	[20]	1×1	-	✓	×	×	×	×	×	<ul style="list-style-type: none"> An ANFIS controller is used in training neural network to detect the abnormality in PV grid connected systems. 	<ul style="list-style-type: none"> AI approaches demand a large amount of data to train the neural network.
	[22]	10×4	-	✓	×	×	×	×	×	<ul style="list-style-type: none"> Short circuit and string level open circuit fault is detected by training the neural network. 	<ul style="list-style-type: none"> Discrimination of PV faults has not been experimented.
	[23]	6.3kW, 433kW	-	✓	×	×	×	×	×	<ul style="list-style-type: none"> An hourly level fault monitoring is employed via unsupervised learning. 	<ul style="list-style-type: none"> Instant fault detection or 100% accurate tripping is not guaranteed.
FBD	[25]	7×7	-	✓	✓	×	×	✓	×	<ul style="list-style-type: none"> PV array and string faults are detected. However, discriminating LL, OC and shade conditions are not considered. 	<ul style="list-style-type: none"> Dependency to datasheet data is seen.
	[26]	14×2, 15×2-2No's	-	✓	×	×	×	×	×	<ul style="list-style-type: none"> An OPC platform is used for remote monitoring PV faults in grid connected systems. 	<ul style="list-style-type: none"> V_{OC} and I_{SC} data in most of the techniques become a mandatory obligation.
	[27]	Ref [27]	-	✓	✓	×	×	✓	✓	<ul style="list-style-type: none"> Shade condition, bypassed module faults, and string level faults are detected. 	<ul style="list-style-type: none"> The catastrophic LL/LG faults are not discussed in most of the works.
	[28]	2×1 – 2No's	-	✓	✓	×	×	✓	✓	<ul style="list-style-type: none"> Ratio based fault detection is proposed for bypass diode fault, OC fault and shade conditions. 	<ul style="list-style-type: none"> Discrimination of temporary and permanent PV faults was not experimented.
FD-ACB based fault detection	-	(4×4) 3 sub-arrays	Electronic switches	✓	✓	✓	✓	✓	✓	<ul style="list-style-type: none"> Fault ratios are proposed to detect the abnormality and the nature of PV fault is accurately predicted using FD-ACB. Enhanced safety and facilitated maintenance are its notable advantages. For various PV operating conditions are easily discriminated with three data samples, which is a plus with FD-ACB setup. 	<ul style="list-style-type: none"> The reference value for fault ratios is formulated only based on three various PV sub-arrays. In this case, the method has a limitation to protect PV sub-array, when all three arrays exhibit the fault conditions.

DET-detection, DISC-discrimination, WPS- wireless self -powered sensor, RPP – Right Power Peak

PV panels, protection devices, and power converters. Conventional PV methods, such as IBM, SBM, and AIT, often require costly microcontrollers, string, and module-level voltage sensors, which increase the overall cost. In contrast, the proposed method only requires electronic switches to improve safety standards. Moreover, the proposed fault detection scheme ensures instantaneous fault detection, providing added cost-effectiveness.

- Fault Recognition Time:** Apart from the SBM, most of the methods in the literature have a significant delay in fault detection, and instant tripping of the MCB is not guaranteed. Conversely, the proposed fault detection

scheme promptly verifies faults using VFR and CFR, enabling immediate MCB tripping and inverter isolation.

- Fault Detection and Discrimination:** Fault detection and discrimination are crucial processes for ensuring safety and maintenance. While existing methods in the literature lack the ability to accurately and simultaneously discriminate between the faults of LL, OC, and PS and the normal operating conditions, the proposed method, the proposed scheme implemented using FD-ACB offers the capability to discriminate between these faults within three data samples. This significantly enhances PV maintenance practices.

The comprehensive comparison of the proposed fault detection scheme highlights its unique features and advantages over existing literature. The commercialization potential, cost-effectiveness, instantaneous fault recognition, and robust fault detection and discrimination capabilities make the proposed method a promising solution for enhancing the safety and reliability of PV power generation systems.

VII. CONCLUSION

This research proposes a new fault detection and discrimination scheme for a large PV system with multiple sub-arrays. Witnessing the *I-V* characteristics change in fault cases, a new FD-ACB is developed and applied to diagnose PV faults conditions. The occurrences of the PS events and the LL, LG, and OC faults are critically evaluated by a threshold in the MPP operation and then appraised by using the proposed FD-ACB. It is a notable contribution of this research that the occurrence of the LL and LG faults with minimal probability can be accurately detected by the proposed scheme. Moreover, regardless of existing protection schemes, the undetected and pre-existing faults can be accurately diagnosed by the proposed scheme without additional sensors, rendering it a cost-effective solution for large PV systems. Unlike current protection schemes requiring a large amount of data, the proposed scheme can determine PV faults with minimal data samples, thus offering a new paradigm for PV system operation and maintenance. Overall, the proposed scheme is found economical, accurate, cost-effective, and reliable solution to overcome the challenges in the protection of large PV systems.

REFERENCES

- [1] D. S. Pillai and N. Rajasekar, "A comprehensive review on protection challenges and fault diagnosis in PV systems," *Renew. Sustain. Energy Rev.*, vol. 91, pp. 18–40, Aug. 2018.
- [2] D. S. Pillai and N. Rajasekar, "Metaheuristic algorithms for PV parameter identification: A comprehensive review with an application to threshold setting for fault detection in PV systems," *Renew. Sustain. Energy Rev.*, vol. 82, Elsevier Ltd, pp. 3503–3525, Feb. 01, 2018.
- [3] Z. Zou, Y. Hu, and B. Gao, "Temperature recovery from degenerated infrared image based on the principle for temperature measurement using infrared sensor," *J. Appl. Phys.*, vol. 115, p. 43522, 2014.
- [4] T. Takashima *et al.*, "Experimental studies of fault location in PV module strings," *Sol. Energy Mater. Sol. Cells*, vol. 93, no. 6–7, pp. 1079–1082, Jun. 2009.
- [5] R. Anil Kumar, M. S. Suresh, and J. Nagaraju, "Measurement of AC Parameters of Gallium Arsenide (GaAs/Ge) Solar Cell by Impedance Spectroscopy," *IEEE Trans. Electron Devices*, vol. 48, no. 9, 2001.
- [6] Y. Hu *et al.*, "Online Two-Section PV Array Fault Diagnosis With Optimized Voltage Sensor Locations," *IEEE Trans. Ind. Electron.*, vol. 62, no. 11, pp. 7237–7246, 2015.
- [7] P. Guerriero *et al.*, "Monitoring and Diagnostics of PV Plants by a Wireless Self-Powered Sensor for Individual Panels," *IEEE J. Photovolt.*, vol. 6, no. 1, 2016.
- [8] L. Chen, S. Li, and X. Wang, "Quickest Fault Detection in Photovoltaic Systems; Quickest Fault Detection in Photovoltaic Systems," *IEEE Trans. Smart Grid*, vol. 9, no. 3, p. 1835, 2018.
- [9] B. P. Kumar *et al.*, "Identification and Localization of Array Faults With Optimized Placement of Voltage Sensors in a PV System," *IEEE Trans. Ind. Electron.*, vol. 68, no. 7, p. 5921, 2021.
- [10] M. Zakir, H. A. Sher, A. Arshad, and M. Lehtonen, "A fault detection, localization, and categorization method for PV fed DC-microgrid with power-sharing management among the nano-grids," *Int. J. Electr. Power Energy Syst.*, vol. 137, p. 107858, May 2022.
- [11] A. F. Murtaza, M. Bilal, R. Ahmad, and H. A. Sher, "A Circuit Analysis-Based Fault Finding Algorithm for Photovoltaic Array Under L-L/L-G Faults," *IEEE J. Emerg. Sel. Top. POWER Electron.*, vol. 8, no. 3, 2020.
- [12] R. Surov, M. K. Alam, J. Johnson, and J. Flicker, "An Irradiance-Independent, Robust Ground-Fault Detection Scheme for PV Arrays Based on Spread Spectrum Time-Domain Reflectometry (SSTDR)," *IEEE Trans. POWER Electron.*, vol. 33, no. 8, 2018.
- [13] M. Ma, Z. Zhang, P. Yun, Z. Xie, H. Wang, and W. Ma, "Photovoltaic module current mismatch fault diagnosis based on I-V Data," *IEEE J. Photovolt.*, vol. 11, no. 3, pp. 779–788, 2021.
- [14] H. A. Abd el-Ghany, A. E. ELGeby, and I. B. M. Taha, "A new monitoring technique for fault detection and classification in PV systems based on rate of change of voltage-current trajectory," *Int. J. Electr. Power Energy Syst.*, vol. 133, Dec. 2021.
- [15] B. P. Kumar *et al.*, "Online Fault Detection and Diagnosis in Photovoltaic Systems Using Wavelet Packets" *IEEE J. Photovolt.*, vol. 8, no. 1, 2018.
- [16] D. S. Pillai and N. Rajasekar, "An MPPT-based sensorless line-line and line-ground fault detection technique for pv systems," *IEEE Trans. Power Electron.*, vol. 34, no. 9, pp. 8646–8659, Sep. 2019.
- [17] P. K. Boggarapu *et al.*, "Identification of Pre-existing/Undetected Line-to-Line Faults in PV Array Based on Preturm on/off Condition of the PV Inverter," *IEEE Trans. Power Electron.*, vol. 35, no. 11, pp. 11865–11878, 2020.
- [18] M. W. Ahmad *et al.*, "A Fault Diagnosis and Postfault Reconfiguration Scheme for Interleaved Boost Converter in PV-Based System," *IEEE Trans. Power Electron.*, vol. 36, no. 4, pp. 3769–3780, 2021.
- [19] D. Xu and H. Chen, "Fault-tolerant strategy without redundant switches for PV systems based on differential power processing converters," *Sol. Energy*, vol. 230, pp. 365–375, Dec. 2021.
- [20] M. Abbas and D. Zhang, "A smart fault detection approach for PV modules using Adaptive Neuro-Fuzzy Inference framework," *Energy Reports*, vol. 7, pp. 2962–2975, Nov. 2021.
- [21] M. Bacha and A. Terki, "Diagnosis algorithm and detection faults based on fuzzy logic for PV panel," *Mater. Today Proc.*, vol. 51, pp. 2131–2138, Jan. 2022.
- [22] R. G. Vieira *et al.*, "Comparing multilayer perceptron and probabilistic neural network for PV systems fault detection," *Expert Syst. Appl.*, vol. 201, p. 117248, Sep. 2022.
- [23] J. Qu *et al.*, "An unsupervised hourly weather status pattern recognition and blending fitting model for PV system fault detection," *Appl. Energy*, vol. 319, p. 119271, Aug. 2022.
- [24] J. J. Chavez *et al.*, "S-Transform based fault detection algorithm for enhancing distance protection performance," *Int. J. Electr. Power Energy Syst.*, vol. 130, p. 106966, Sep. 2021.
- [25] G. G. Kim *et al.*, "Fault Detection for Photovoltaic Systems Using Multivariate Analysis With Electrical and Environmental Variables," *IEEE J. Photovolt.*, vol. 11, no. 1, 2021.
- [26] S. Silvestre *et al.*, "Remote supervision and fault detection on OPC monitored PV systems," *Sol. Energy*, vol. 137, pp. 424–433, Nov. 2016.
- [27] S. Silvestre *et al.*, "New procedure for fault detection in grid connected PV systems based on the evaluation of current and voltage indicators," *Energy Convers. Manag.*, vol. 86, pp. 241–249, Oct. 2014.
- [28] I. Yahyaoui and M. E. V. Segatto, "A practical technique for on-line monitoring of a photovoltaic plant connected to a single-phase grid," *Energy Convers. Manag.*, vol. 132, pp. 198–206, Jan. 2016.
- [29] J. P. Ram *et al.*, "Design and overview of maximum power point tracking techniques in wind and solar photovoltaic systems: A review," *Renew. Sustain. Energy Rev.*, vol. 73, no. Nov.2016, pp. 1138–1159, 2017.
- [30] D. S. Pillai *et al.*, "An Accurate, Shade Detection-Based Hybrid Maximum Power Point Tracking Approach for PV Systems," *IEEE Trans. Power Electron.*, vol. 35, no. 6, pp. 6594–6608, 2020.